

# 1 Modelling, simulation and comparison of phase change material storage 2 based direct and indirect solar organic Rankine cycle systems

3 Jahan Zeb Alvi<sup>1</sup>, Yongqiang Feng<sup>1\*</sup>, Qian Wang<sup>1\*\*</sup>, Muhammad Imran<sup>2</sup>, Junaid Alvi<sup>3</sup>

4 <sup>1</sup>*School of Energy and Power Engineering, Jiangsu University, 301 Xuefu Road, Zhenjiang, China*

5 <sup>2</sup>*Mechanical Engineering & Design, School of Engineering and Applied Science, Aston University, Aston  
6 Triangle, B4 7ET, Birmingham, United Kingdom*

7 <sup>3</sup>*Key Laboratory of Efficient Utilization of Low and Medium Grade Energy, MOE, School of Mechanical  
8 Engineering, Tianjin University, Tianjin 300072, China*

9 *\*Corresponding author: Dr. Yongqiang Feng, Prof. Qian Wang*

10 *Email ID: [hittfengyq@gmail.com](mailto:hittfengyq@gmail.com), [qwang@ujs.edu.cn](mailto:qwang@ujs.edu.cn)*

## 11 Abstract

12 The thermodynamic performance of a novel direct solar organic Rankine cycle system and conventional  
13 indirect solar organic Rankine cycle system is compared in this study. The working fluid is vaporized  
14 directly in the solar collectors in direct solar organic Rankine cycle system while heat transfer fluid is  
15 used to vaporize the working in indirect solar organic Rankine cycle system. The evacuated flat plate  
16 collectors array covering a total aperture area of 150 m<sup>2</sup> is employed as a heat source and a phase change  
17 material tank having a surface area of 25.82 m<sup>2</sup> is used as thermal storage for both configurations.  
18 R245fa and water are chosen as heat transfer fluids for direct and indirect solar organic Rankine cycle  
19 systems, respectively. However, R245fa is used as a working fluid for both configurations. The  
20 performance of both configurations is compared by carrying out weekly, monthly and annual dynamic  
21 simulations in MATLAB by using hourly weather data of Islamabad, Pakistan. The direct solar organic  
22 Rankine cycle system outperforms the indirect solar organic Rankine cycle system in terms of thermal  
23 efficiency and net power. The annual system efficiency and an annual average net power of the direct  
24 solar organic Rankine cycle system are 71.96% and 64.38% higher than indirect solar organic Rankine  
25 cycle system respectively. However, average annual heat stored by phase change material during  
26 charging mode of indirect solar organic Rankine cycle system is 4.24 MJ more than direct solar organic  
27 Rankine cycle system. Conversely, direct solar organic Rankine cycle system has provided annual daily  
28 average power of 33.80 kW extra to heat transfer fluid during the discharging mode of phase change  
29 material storage. Furthermore, with phase change material storage, the capacity factor is increased by  
30 17 % and 21.71 % on annual basis for direct and indirect solar organic Rankine cycle systems,  
31 respectively.

32

33 **Keywords:** Organic Rankine Cycle; Direct and Indirect solar ORC system; Phase Change Material;  
34 Capacity Factor; Thermodynamic, Comparison

## 36 **1 Introduction**

37 Solar energy has emerged as one of the most rapidly growing renewable sources of electricity. It has a  
38 minimum time of replenishment and maximum capacity among all available energy resources [1].  
39 Furthermore, it is an attractive option for coupling with a low-medium temperature organic Rankine  
40 cycle (ORC) system. A temperature of 100 °C or slightly higher is enough to run a solar ORC system.  
41 Hence, these solar ORC systems are able to work efficiently within a temperature range of 100 to 150  
42 °C. They are beneficial in terms of power, all the way down to small unit sizes, low technical demand  
43 in heat storage, co-generation close to the usage point and suitability in regions with less direct solar  
44 radiation resources.

45 To date, most of the studies investigated solar ORC systems use heat transfer fluid (HTF) to transfer  
46 energy from collectors to the organic fluid [2–5]. Heat transfer irreversibility largely occurs in the  
47 evaporator as explained by Jing et al. [6]. Furthermore, investment cost also increases while using  
48 HTF. Extra power is required for the pumping of HTF that can decrease the system's net power output  
49 specifically for small-scale solar ORC systems. The direct solar organic Rankine cycle system (DSOS)  
50 is one in which the evaporator is replaced with the solar collectors. Hence, all of the aforementioned  
51 problems can be resolved by adopting the novel DSOS.

52 To date, the solar ORC system with direct vapor generation (DVG) is studied by different researchers.  
53 Few have conducted experimental work [7,8] while others have done theoretical studies [6,9,10]. All  
54 of them focused on working fluid selection and performance of the system. This kind of system is found  
55 to be promising. In DVG solar ORC system vapor is generated directly in the collectors, the working  
56 fluid influences not only the heat to power conversion but also the solar energy collection.

57 Jing et al. [6] explained heat transfer irreversibility largely occurs in the evaporator. Moreover, they  
58 found 10% relative increment in overall electricity efficiency of DVG based solar ORC over  
59 conventional solar ORC system at solar radiation of 1000 W/m<sup>2</sup>. Furthermore, extra power is required  
60 for the pumping of HTF in conventional solar ORC that can decrease the system's net power output and  
61 overall system efficiency specifically for small-scale solar ORC systems. Freeman et al. [23] calculated  
62 that almost 58% of the exergy loss occurs in the evaporator.

63 The thermal energy storage is a core component in the development of a solar power system. Thermal  
64 energy storage for solar thermal applications can be divided into Latent Heat Storage (LHS) and  
65 Sensible Heat Storages (SHS) [11]. Phase Change Materials (PCMs) lies into the LHS group and are  
66 one of the promising technology for the development of efficient thermal storage. Moreover, 5–14 times  
67 additional energy per volume can be stored by using PCM as compared to sensible-heat storage  
68 materials [12]. PCM is also advantageous compared with SHS systems because the process of phase

69 change is nearly isothermal for pure substances, and takes place over a finite temperature range for  
70 composite materials [13,14]. In contrast, past research had shown some disadvantages of PCM related  
71 to low thermal conductivity which results in lower charging and discharging rates [15]. PCMs are  
72 classified into three different transition phases such as liquid to solid, solid to gas and solid to liquid.  
73 The solid-liquid transition can be further subdivided into organic, inorganic and eutectics [12,16]. The  
74 selection of PCM to make the best latent heat storage system is critical for the specific application since  
75 the operating conditions are widely variable. The melting point temperature is a key parameter in the  
76 selection process of PCM. An overview of the PCM properties and related applications are studied by  
77 Agyenim et al. [14]. The applications are subdivided into low temperature (1-65 °C), medium  
78 temperature (80-120 °C) and high temperature (>150 °C). Medium temperature range PCMs are suitable  
79 for solar ORC applications.

80 Previously, researchers have proposed and analyzed different configurations of solar ORC systems.  
81 However, few of them have focused on integrating the systems with heat storage. Li et al. [17] analyzed  
82 solar organic Rankine cycle with thermal energy storage. A dynamic model of the solar ORC system  
83 was developed. The effect of storage capacity, solar fluctuation and evaporation temperature on the  
84 solar ORC system were evaluated. It was concluded that a proper thermal energy storage capacity  
85 should be selected in order to cater the solar fluctuations of a given area. Wang et al. [3] investigated  
86 the off-design performance of the solar ORC system with the compound parabolic collector and sensible  
87 thermal storage unit. The system performance was observed under time-varying conditions and  
88 changing ambient temperature. The system could obtain maximum exergy efficiency in December  
89 while maximum power output in June. Freeman et al. [18] had studied domestic-scale distributed solar  
90 combined heat and power system consisting of an organic Rankine cycle for the UK climate. The system  
91 comprised of 15 m<sup>2</sup> solar collectors, 1 m<sup>3</sup> thermo-chemical storage, and ORC engine. Two staged solar  
92 collectors were considered. It was found that the proposed system could meet 32 % electricity demands  
93 of a UK home. The author suggested that future studies will be focused on providing a proper solution  
94 of a finite-sized thermal storage system. Moreover, the effectiveness of the storage system will be  
95 assessed for load profile matching over seasonal time-scales. Wang et al. [19] developed a mathematical  
96 model to simulate the solar ORC system under steady-state. It was concluded that by employing a heat  
97 storage unit into the system, uninterrupted and steady operation of the solar-driven regenerative organic  
98 Rankine cycle could be achieved over a long period of time.

99 Pantaleo et al. [20,21] carried out two different studies on ORC coupled with heat storage. In the first  
100 study, the heat was recovered from exhaust gasses of gas turbine via thermal energy storage. Two  
101 molten salts storage tanks of (one cold at 200 °C and one hot at 370 °C) and three different plant  
102 locations were selected. The thermodynamic modelling was performed assuming two CSP sizes, and  
103 consequently two thermal energy storage sizes. The thermodynamic performance indicated higher  
104 global energy conversion efficiencies while using CSP integration. The second study was focused on

105 thermodynamic modelling and chosen two different CSP sizes, storage levels, and operation modes.  
106 Two molten salt storage tanks were considered which provided the 4.8–18 MWh energy storage. The  
107 plant capacity factor was increased and operating hours increased from 5500–6000 to 8000 h per year.

108 The integration of ORC with the PCM storage unit has gained attention in the recent past. Gang et al.  
109 presented two different configurations [22,23] of the solar ORC system with PCM storage unit. The  
110 first study was focused on the comparison of a regenerative ORC with the solo cycle. The system  
111 consists of non-tracking solar collectors and ORC engine integrated with a PCM storage tank. The  
112 research was focused on the effect of the regenerative cycle on system efficiency and collector  
113 efficiency. However, the second study was focused on the arrangement of the two-stage solar collectors.  
114 Flat plate collectors with corresponding PCM storage were used for preheating. Compound parabolic  
115 concentrators with corresponding PCM storage were used to achieve a higher temperature. Furthermore,  
116 collector efficiency and overall cycle efficiency were calculated.

117 Freeman et al. [24] proposed different thermal energy solutions. Authors applied various combinations  
118 of PCMs storage, water storage and solar collectors in a small-scale solar organic Rankine cycle  
119 combined heat and power system. Their performance was evaluated for UK and Cyprus climates,  
120 respectively. Furthermore, PCMs resulted in a 20% higher total daily electrical output per unit storage  
121 volume as compared to water storage.

122 Marcello et al. [25] analyzed and compared different PCMs coupled with the ORC system. It was found  
123 that the amount of energy stored and the thermal efficiency of the system increased with increasing heat  
124 source temperature. Conclusively, it was observed that the amount of energy stored by PCM increased  
125 dramatically by using a metal foam. This happened due to the higher thermal conductivity of the foam  
126 which resulted in the faster melting process. Manfrida et al. [26] and Sagar et al. [27] integrated PCM  
127 storage with solar ORC system. Their studies were focused on developing a mathematical model of  
128 PCM storage. Then dynamic simulations of overall systems were carried out for seven and ten days,  
129 under time-varying weather conditions (solar radiation, ambient temperature), for first and second study  
130 respectively. In case of first study, the model gave time-dependent HTF temperature profile of PCM  
131 storage tank outlet. It was then applied to solar ORC system. Weekly average energy efficiency  
132 achieved by the PCM storage was 83% during charging mode and 93% during discharging mode,  
133 respectively. Two different diameters and lengths of PCM storage tank were selected in the second  
134 study. It was found that smaller diameter and longer length showed the overall better performance of  
135 solar ORC system. In contrast, the pressure drop was significantly high for aforementioned system.

136 However, previous studies mainly focused on the design and short-time simulations. Detailed modeling  
137 and simulation of integrated direct solar organic Rankine cycle system and direct solar organic Rankine  
138 cycle system (ISOS) for a whole year had not been reported yet. The novelty of this work lies in the  
139 thermodynamic performance assessment and comparison of the performance of DSOS and ISOS based

140 on the thermodynamic model. The contribution includes

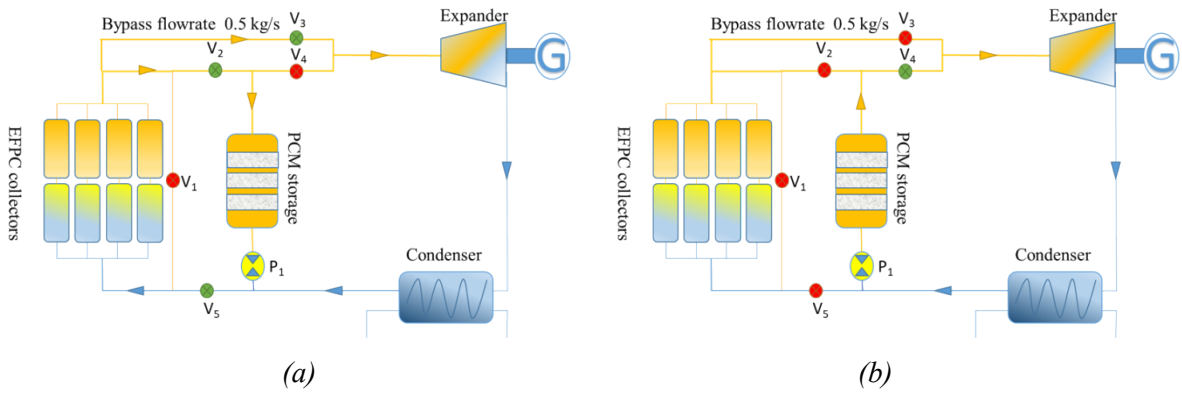
- 141 • Development and validation of the 1-dimensional PCM model for integrated solar ORC system.  
142 Temperature profiles of both HTF and PCM are demonstrated and compared for the first time  
143 under time-varying weather conditions.
- 144 • The weekly, monthly and annual dynamic simulations of the integrated solar ORC system in  
145 relation to the charging and discharging characteristics of the PCM storage system.  
146 Furthermore, increment in the capacity factor of both configurations by using PCM storage is  
147 also analyzed and compared for the first time.
- 148 • Thermodynamic performance and comparative assessment of DSOS and ISOS based on system  
149 efficiencies and net power output.

150 The present study is divided into five sections. [Section 1](#) of the paper provides an overview of the  
151 current research status in the area of solar organic Rankine cycle (ORC) system with a focus on novelty  
152 and originality of the present work. The layout, working principle, and control of the integrated solar  
153 ORC system presented in [Section 2](#). The modelling and simulation approach is described in detail in  
154 [Section 3](#). The results and discussion of the DSOS and ISOS are provided in [Section 4](#). Finally, the  
155 concluding remarks are added in [Section 5](#) of the paper.

## 156 2 System configurations and control

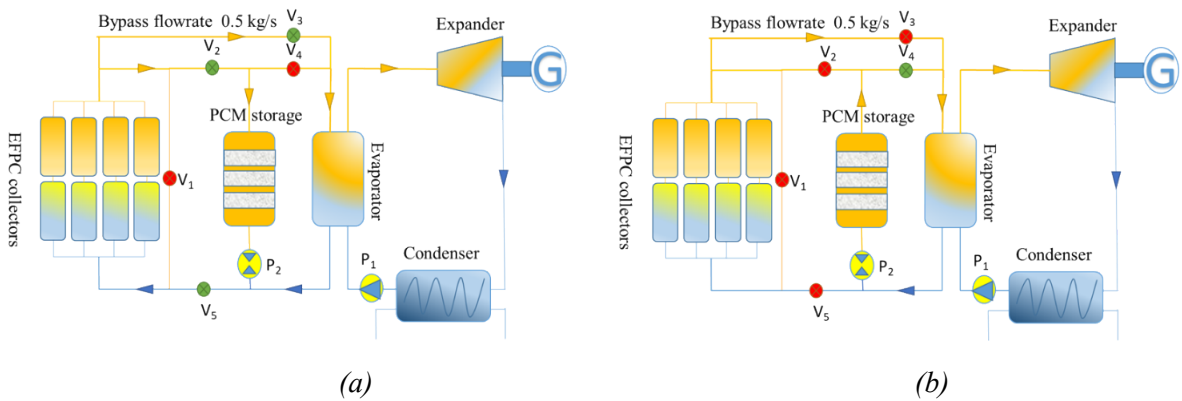
157 The schematic diagrams of the DSOS and ISOS are shown in [Figure 1](#) and [Figure 2](#), respectively.  
158 Present work has been carried out to compare the performance of both configurations on the basis of  
159 hourly weather data. Both configurations are comprised of evacuated flat plate collectors (EFPCs),  
160 phase change material storage tank and basic ORC plant (evaporator, expander, condenser, and pump)  
161 coupled with a generator. PCM storage works in two operating modes (charging mode & discharging  
162 mode). In the case of DSOS, solar collectors work as an evaporator during charging mode as shown in  
163 [Figure 1](#). However, during the discharging mode, the PCM storage tank works as an evaporator. One  
164 variable flow organic fluid flow pump namely  $P_1$  is employed to regulate fluid flow in the system. HTF  
165 is replaced by organic fluid in this system. Moreover, R245fa is used as a working fluid.

166 In the case of ISOS, water works as HTF in the solar loop while R245fa is used as a working fluid ORC  
167 loop as shown in [Figure 2](#). Moreover, two variable flow pumps entitled  $P_1$  and  $P_2$  are employed to  
168 control the flow of HTF & working fluid in solar and ORC loop respectively. Five control valves are  
169 also used to properly regulate the flow of fluid in both configurations. The valves open and close based  
170 on the operation and control conditions, which are discussed in detail in the section below. Both  
171 configurations integrated with PCM storage are simulated in MATLAB programming environment  
172 under time-varying solar radiation conditions.



173  
174

175 *Figure 1: Layout diagram of direct solar organic Rankine cycle system (DSOS) during (a) charging*  
176 *mode and (b) discharging mode*



177  
178

179 *Figure 2: Layout diagram of indirect solar organic Rankine cycle system (ISOS) during (a) charging*  
180 *mode and (b) discharging mode*

181 Hourly based climatic data of Islamabad-Pakistan has been used for the current study. Typical  
182 meteorological year (TMY) data of Islamabad is obtained by using Meteonorm software [28].  
183 Islamabad represents cold winter and very hot and hot-humid summer. The monthly average ambient  
184 temperature along with the solar radiation falling on the solar collector surface for the whole year is  
185 shown in [Figure 3](#). It can be observed that June is the hottest month with the maximum amount of solar  
186 radiation and maximum ambient temperature while January is the coldest month of the year along with  
187 low solar radiation and minimum ambient temperature. The first week of January and the second week  
188 of June are considered to be the coldest and hottest weeks of the whole year, respectively.

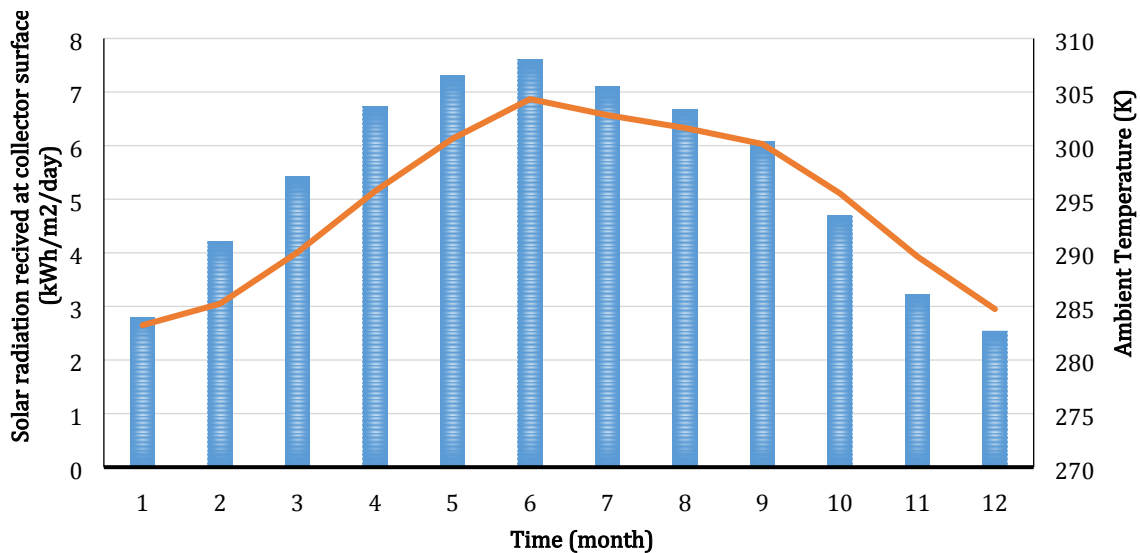


Figure 3: Climatic data of Islamabad- Pakistan (daily average monthly)

189

190

191 To apply the desired logical control system, every component for both configurations is controlled and  
 192 turned on and off by logical functions depending on several simulation parameters. The values of TMY  
 193 data of the Islamabad is imported in MATLAB from the metronome software. Both configurations have  
 194 been evaluated at the same operation and boundary conditions. It is assumed that the system starts  
 195 working when the solar radiation received at the surface of the collector goes above  $400 \text{ W/m}^2$ . On the  
 196 contrary, the system stops or undergoes to discharging mode.

197 There are two modes of operation of the storage system namely charging and discharging mode. The  
 198 initial temperature of PCM is assumed to be  $373.15 \text{ K}$ . This shows that PCM is not charged and in the  
 199 solid phase at the beginning of the simulation process. Five control valves are employed in both  
 200 configurations which are opened and closed depending upon the mode of operation. During charging  
 201 mode, valves V2, V3 and V5 are opened while V1 and V4 remain close. In contrast, during the  
 202 discharging mode, V4 is opened while the rest of the valves remains close. The heat storage system is  
 203 designed to work at melting point temperature of the PCM. It means that major part of the energy is  
 204 released or absorbed at the melting point of PCM.

205 The maximum temperature at the outlet of collector array is selected to be  $390 \text{ K}$  that is slightly higher  
 206 than the PCM melting point temperature. In this regard, when the collector outlet temperature rises  
 207 above the limit imposed, V1 is opened and the rest of valves are closed and the HTF mass flow rate is  
 208 increased by  $10\%$  at every iteration until it reaches below the limit imposed. To avoid the supercritical  
 209 condition, Initial temperature of HTF mass flow rate during charging mode is selected to be  $3 \text{ kg/s}$  and  
 210 it increases with increment in collector outlet temperature. However, to achieve consistent power  
 211 generation, HTF bypass mass flow rate is kept at a constant rate of  $0.5 \text{ kg/s}$  in both charging and  
 212 discharging mode. The discharging limit of the storage tank is maintained to  $370 \text{ K}$ , which means that  
 213 the system is allowed to discharge the storage in sensible heat region.

## 214 3 Thermodynamic modelling

### 215 3.1 Solar radiation

216 Solar radiation received by the sloped surface of the solar collectors is calculated by [29].

217

$$I_t = \left( I_b + I_d \frac{I_b}{I_h} \right) R_b + I_d \left( 1 - \frac{I_b}{I_h} \right) \left( \frac{1 + \cos \beta}{2} \right) \left( 1 + \sqrt{\frac{I_b}{I_h}} \sin^3 \left( \frac{\beta}{2} \right) \right) + I_h \rho_g \left( \frac{1 - \cos \beta}{2} \right) \quad (1)$$

218

### 219 3.2 Solar collectors

220 For the solar collector's field, evacuated flat plate collectors are selected. Due to vacuum inside the  
221 collector, this type of collector is highly efficient at high temperatures up to 200°C. Moreover, they are  
222 non-tracking, non-concentrating collectors. Therefore, they do utilize both beam and diffused radiation  
223 [30]. The efficiency of the solar collector is calculated as a function of collector inlet temperature, the  
224 ambient air temperature and total solar radiation received at collector surface.

225

$$\eta_{cl} = a_0 - a_1 \frac{(T_i - T_{amb})}{I_t} - a_2 \frac{(T_i - T_{amb})^2}{I_t} \quad (2)$$

226

227

228 Where  $a_0$ ,  $a_1$  and  $a_2$  are the optical efficiency of the collector, linear heat loss coefficient, and quadratic  
229 heat loss coefficient, respectively. A total number of solar collectors were assumed to be 75 in collector  
230 array and each solar collector has a size of 2 m<sup>2</sup>. Amount of energy received by the solar collector's  
231 array is computed by:

232

$$q_{cl} = \eta_{cl} \times I_t \times n \times A_{cl} \quad (3)$$

233 Furthermore, the temperature at the outlet of the solar collector array is calculated by

234

$$T_o = T_i + \left( \frac{q_{cl}}{(m_f C_p)} \right) \quad (4)$$

### 235 3.3 Phase change material storage

236 [Figure 4](#) shows a typical configuration of the PCM storage tank. A cylindrical shape tank completely  
237 filled with PCM is considered. Moreover, it has a coiled shape pipe containing HTF passes through the  
238 tank. The walls of the PCM storage tank are assumed to be adiabatic.

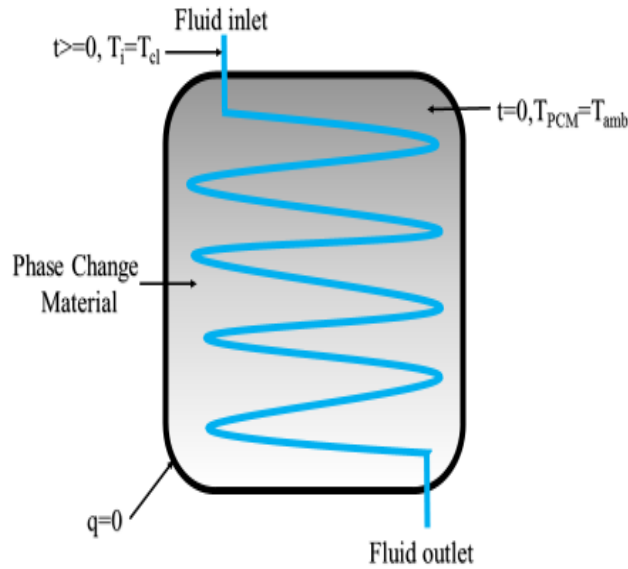
239 The tank operates in charging and discharging mode depending upon operation and boundary  
240 conditions. During charging mode, the heat is transferred from HTF to the PCM. The PCM temperature  
241 rises from solid-phase until it reaches the melting point temperature. After that, the temperature of PCM



242 remains constant during the melting process.

243 After completion of the melting phase during which all of the PCM changes into the liquid phase, the  
 244 temperature of the liquid PCM further rises up to the limit imposed by HTF. However, during a  
 245 discharging phase, thermal energy stored by liquid PCM is extracted by cold HTF [26]. The well-known  
 246 enthalpy method is used to solve the governing equations for HTF and PCM as shown in equation (5)  
 247 [31][32]. In order to determine the heat transfer in PCM while solving the enthalpy method few  
 248 assumptions are made as follows:

- 249 • Conductive heat transfer is considered to be the dominant mechanism.
- 250 • Only One-dimensional heat transfer is contemplated.
- 251 • The thermos-physical properties of PCM remain constant for each state.
- 252 • Natural convection is neglected in this model which may occur due to the density difference in  
 253 the PCM [33].



254  
 255 *Figure 4: Layout diagram of PCM storage Tank*

256

$$\rho \frac{\partial H}{\partial t} = \kappa_{pcm} \frac{\partial^2 T_{pcm}}{\partial y^2} \quad (5)$$

257 Where “H” is the total volumetric enthalpy, which consists of both the latent heat and the sensible heat  
 258 of PCM at a given temperature. Therefore, the total volumetric enthalpy of PCM at any given  
 259 temperature is calculated using the following relation:

260

$$H = \int_{T_m}^T \rho_{pcm} c_{pcm} \Delta T_{pcm} + \rho_{pcm} L F(\lambda) \quad (6)$$

261

262 In the above formulation equation (6), the latent heat of the PCM is related to the liquid fraction of the

263 PCM “LF”. To compute the latent heat of the PCM, the liquid fraction LF needs to be defined that is  
 264 calculated as given by the Equation (7)

$$265 \quad LF = \begin{cases} 0 & \text{for } T_{pcm} < T_m \text{ Solid region} \\ 1 & \text{for } T_{pcm} > T_m \text{ Liquid region} \end{cases} \quad (7)$$

266  
 267 From equation (6) and (7) enthalpy of PCM can be calculated as:

$$268 \quad H = \begin{cases} \rho_{pcm} C_{pcm} (T_{pcm} - T_m) & \text{for } T_{pcm} < T_m \text{ Solid region} \\ \rho_{pcm} C_{pcm} (T_{pcm} - T_m) + \lambda \rho_{pcm} & \text{for } T_{pcm} > T_m \text{ Liquid region} \end{cases} \quad (8)$$

269  
 270 The above correlation depicts, if the temperature of PCM is less than its melting point temperature, it  
 271 only contains sensible heat. Conversely, if the temperature of PCM is more than or equal to its melting  
 272 point temperature, total volumetric enthalpy is the combination of latent heat and sensible heat. The  
 273 temperature of the PCM “ $T_{pcm}$ ” is further derived from the volumetric enthalpy of the PCM as follows:

$$274 \quad T_{pcm} = \begin{cases} T_m + \frac{H}{\rho_{pcm} \cdot C_{pcm}} & \text{for } H < 0 \\ T_m & \text{for } 0 < H < \rho_{pcm} \cdot \lambda \\ T_m + \frac{H - (\rho_{pcm} \cdot \lambda)}{\rho_{pcm} \cdot C_{pcm}} & \text{for } H > \rho_{pcm} \cdot \lambda \end{cases} \quad (9)$$

275 In equation (9)  $\lambda$  is the latent heat of the PCM while  $\rho_{pcm}$  is the density of PCM. The thermophysical  
 276 properties of PCM used in the current study are given in [Table 1](#).

277 *Table 1: Thermo-Physical properties of PCM used for the current study [26]*

Commercial Name	Salt hydrate	
PCM category	Inorganic	
Melting point (K)	389.85	
Latent heat (kJ/kg)	160	
Length of PCM tube (m)	24	
Diameter of PCM tube (m)	0.35	
Thermal conductivity (W/m <sup>2</sup> -K)	both phases	0.7
Specific heat capacity (kJ/kg-K)	both phases	2.61

278  
 279 The amount of energy stored by PCM during the charging mode is calculated by multiplying the mass

280 of the PCM with the difference in latent heat between a final and initial node of the PCM storage tank.

281

$$Q_{st,c} = M_{pcm} (\lambda_{mx} - \lambda_{in}) \quad (10)$$

282

283 Power transferred to HTF by PCM during discharging mode is calculated by equation (11)

284

$$P_{tr,d} = m_{HTF} C_{HTF} (T_{HTF,o} - T_{HTF,i}) \quad (11)$$

285

### 286 3.4 Validation of the Computational Model

287 Currently used PCM computational model has been validated from the experimental results of Zivkovic

288 et al. [33]. Results are presented for the melting case of the PCM. Zivkovic et al. [33] using  $\text{CaCl}_2 \cdot 6\text{H}_2\text{O}$

289 PCM encapsulated in the rectangular container made of stainless steel. The length and breadth of the

290 container are both 100 mm, while the thickness is 20mm, respectively. The container with solid PCM

291 was placed in a bath having a constant temperature of 333.15 K. The PCM container was well insulated

292 on the lateral sides. The experimental results were reproduced through the current computational model.

293 To reproduce the result the convective heat transfer coefficient between air and the container wall is

294 determined by  $h_{\text{conv}}=16 \text{ W/m}^2\text{-K}$  and  $T_{\infty}$  was 333.15 K [33]. Thermophysical properties of the  $\text{CaCl}_2 \cdot$

295  $6\text{H}_2\text{O}$  are tabulated in [Table 2](#).

296

*Table 2: Thermo-Physical properties of  $\text{CaCl}_2 \cdot 6\text{H}_2\text{O}$*

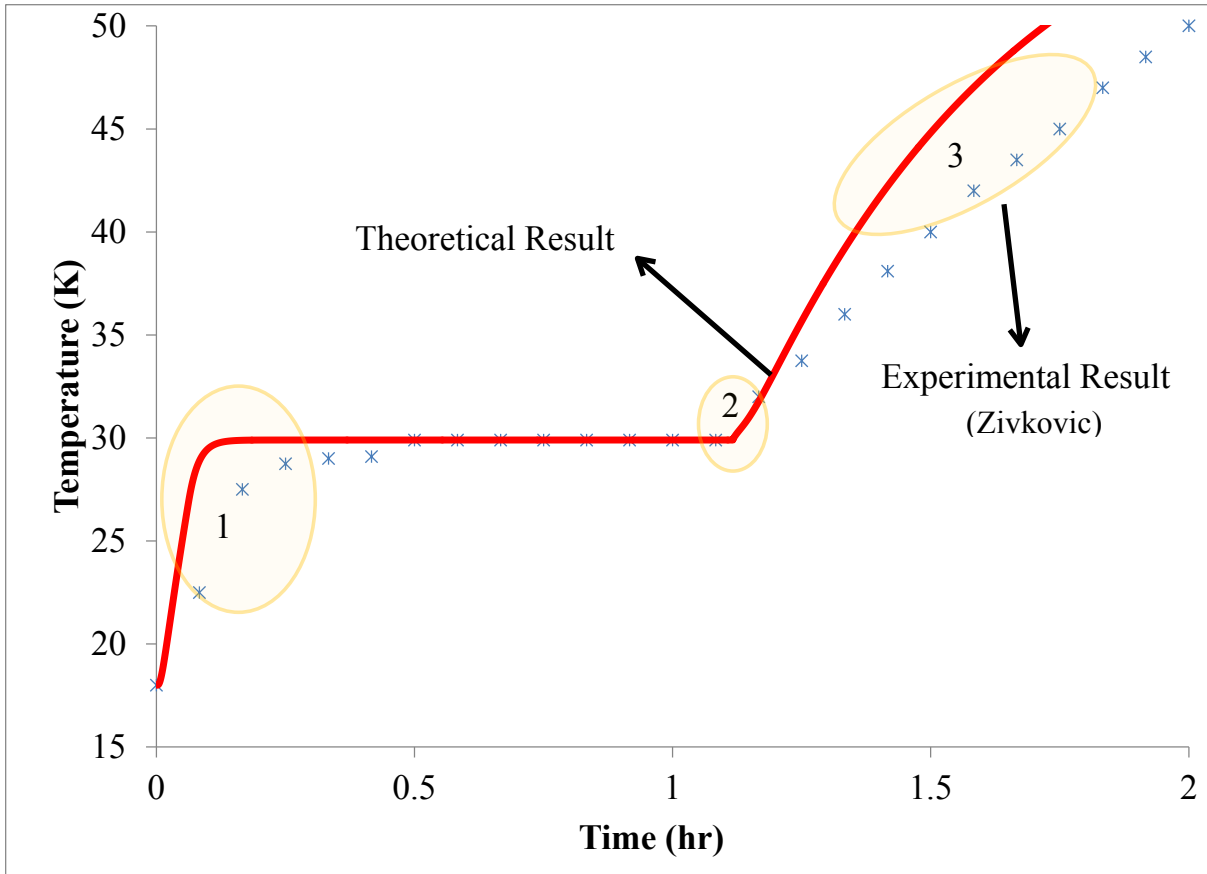
Melting Point (K)		303.05
Latent heat (kJ/kg)		187
Density ( $\text{kg/m}^3$ )	Solid	1710
	Liquid	1530
Thermal conductivity ( $\text{W/m}^2\text{-K}$ )	Solid	1.09
	Liquid	0.53
Specific heat capacity ( $\text{kJ/kg-K}$ )	Solid	1.4
	Liquid	2.2

297

298 A comparison between the experimental results from Zivkovic et al. [33] and the current computational

299 model, for the PCM temperature at the center of the container, is presented in [Figure 5](#).

300



301  
 302 *Figure 5: Comparison of the PCM modeling results with the experimental results of Zivkovic and*  
 303 *Fujii [33] for the melting of PCM.*

304 It has been observed from [Figure 5](#) that agreement is well within the uncertainties indicated by Zivkovic  
 305 et al. [33]. Three major observations and discrepancies (mentioned in [Figure 5](#)) between the predicted  
 306 results and the experimental results are observed that are explained below:

- 307 1. In the beginning, sensible heat released by the PCM was predicted faster compared to the  
 308 experimental result. This is mainly due to the assumption considered in the theoretical model which  
 309 neglects the conduction between the container wall and PCM. This point is indicated as 1 in [Figure](#)  
 310 [5](#).
- 311 2. Calculated PCM melting time is observed slightly higher compared to the experimental result  
 312 which is mainly due to the reason that the natural convection currents within the PCM are not  
 313 incorporated in the theoretical model. This point is indicated as 2 in [Figure 5](#).
- 314 3. The theoretical model predicted the higher temperature in the liquid region compared to the  
 315 experimental results at any time. This discrepancy is indicated as 3 in [Figure 5](#). This mainly due to  
 316 the reasons indicated by Zivkovic et al. [33] that the calculated heat transfer coefficient is a little  
 317 bit higher compared to the real one.

318 Therefore it can be assumed very carefully that avoiding the natural convection and thermal conduction  
 319 of the container wall at this stage may not produce a significant error in the prediction of the PCM

320 temperature.

### 321 3.5 Organic Rankine cycle

322 The basic Organic Rankine Cycle (ORC) configuration is chosen for the current simulation study due  
323 to lower capital investment for low-medium temperature applications [34][35]. The operating  
324 conditions and assumptions for the design of the ORC system are listed in [Table 3](#).

325 *Table 3. Assumptions of the boundary conditions for ORC system design*

Parameter	Value
Hot water (heat source) mass flow rate	0.5 kg/s
Pinch point temperature difference in evaporator and condenser [36]	5 K
Turbine efficiency for initial cycle design [37]	80%
Pump efficiency for initial cycle design [38]	60%
Generator efficiency	85%
Degree of superheating at turbine inlet [39]	3 K
Condensation temperature	303.15 K

326 Properties of the working fluid R245fa are shown in [Table 4](#).

Working fluid	R245fa
Critical temperature	154.01°C
Critical pressure	3.651 MPa
ODP	0
Net GWP	4
Flammability	High

327 The power generated by the expander is calculated by equation (12).

$$W_t = m_{wf} (h_{t,i} - h_{t,o}) \quad (12)$$

328 The total power consumed by the pump is computed by equation (13) and (14) for ISOS and DSOS  
329 respectively.

$$W_p = W_{p1} + W_{p2} \quad (13)$$

330 There is only one pump used in DSOS. Therefore, pump power is given by equation (14)

$$W_p = W_{p1} \quad (14)$$

331

332 Pump power within the ORC cycle is calculated by enthalpy difference across the organic fluid pump.

$$W_{p1} = m_{wf}(h_{p,o} - h_{p,i}) \quad (15)$$

333 However, in the case of ISOS, the power consumed by the pump in the solar loop is calculated by  
334 equation (16) using a fixed value of 65 % for solar pump efficiency  $\varepsilon_{sp}$ .

$$W_{p2} = \frac{m_{HTF} \Delta P}{\varepsilon_{sp} \rho_{HTF}} \quad (16)$$

335

336 The pressure drop  $\Delta P$  comprises the pressure loss in the system's pipe network  $\Delta P_L$  and the pressure  
337 loss across the solar collector array  $\Delta P_{cl}$ . The total length of the pipe network is assumed to be 200 m  
338 and diameter 20 mm. The Darcy friction factor  $f$  associated with pressure drop is computed according  
339 to correlations based on the Reynolds number given in Incropera et al. [40]

$$f = 0.316 \text{Re}^{-1/4}; \quad \text{Re} < 2 \times 10^4; \quad (17)$$

$$f = 0.814 \text{Re}^{-1/5}; \quad \text{Re} \geq 2 \times 10^4; \quad (18)$$

$$\frac{\Delta P_L}{L} = \frac{8 m_{HTF}^2 f}{\pi^2 \rho_{HTF} D^5} \quad (19)$$

340

341 The pressure drop across the solar collector array is calculated by an empirical correlation given by  
342 Freeman et al. [18].

$$\Delta P_{cl} = A_{cl}(21.77 m_{HTF}^2 + 3.54 m_{HTF}) \quad (20)$$

343 The isentropic efficiency of the expander and the pump is defined by equation (21) and (22)

$$\varepsilon_t = \frac{h_{t,i} - h_{t,o}}{h_{t,i} - h_{t,os}} \quad (21)$$

344

$$\varepsilon_p = \frac{h_{p,os} - h_{p,i}}{h_{p,o} - h_{p,i}} \quad (22)$$

345 Where os represents the isentropic process. The energy required in the heating process of the ORC is  
346 calculated by the enthalpy increment of the organic fluid from the pump to the expander.

$$W_{net} = W_t \varepsilon_g - W_p \quad (23)$$

347

348

$$Q_{ORC} = m_{wf} (h_{t,i} - h_{p,o}) \quad (24)$$

349 The ORC efficiency for both configurations is defined by the ratio of the net power output to the heat  
350 supplied [6].

$$\eta_{ORC} = \frac{W_{net}}{Q_{ORC}} \quad (25)$$

351 The system efficiency of both solar ORC systems is expressed by

$$\eta_{sys} = \eta_{ORC} \cdot \eta_{cl} \quad (26)$$

352 The increment in a capacity factor of both configurations is calculated by a relative increment in  
353 working hours by use of PCM storage.

$$CF_{inc} = \frac{Wh_{w,pcm} - Wh_{wo,pcm}}{Wh_{w,pcm}} \quad (27)$$

## 354 4 Results and Discussions

355 Results obtained from dynamic MATLAB simulation of solar ORC systems are presented, analyzed  
356 and discussed in this section. A time step of 1 hour is selected for the whole simulation process.  
357 Islamabad is chosen as a reference location having coordinates: 33.7294° N, 73.0931° E. Whole year  
358 simulations are carried out to compare the performances of both DSOS and ISOS. Firstly, dynamic  
359 simulations are carried out for the coldest and hottest weeks of the year. The performance of PCM  
360 storage is also compared for both DSOS and ISOS during charging and discharging mode.

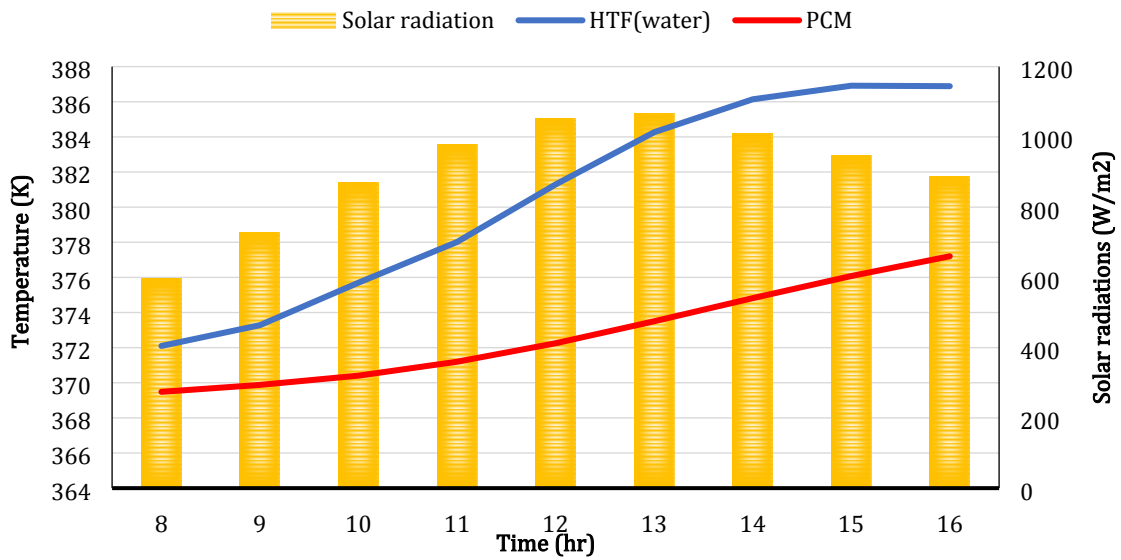
361 Results of system efficiencies of both configurations and net power output are also compared and  
362 discussed. Secondly, the performance of both configurations is compared for the whole year. Moreover,  
363 it is also analyzed how much heat is stored by PCM during charging mode and how much power is  
364 delivered to the PCM by HTF in discharging mode. Finally, an increase in the capacity factor by using  
365 PCM storage for both configurations are presented and analyzed.

### 366 4.1 Performance of the hottest week

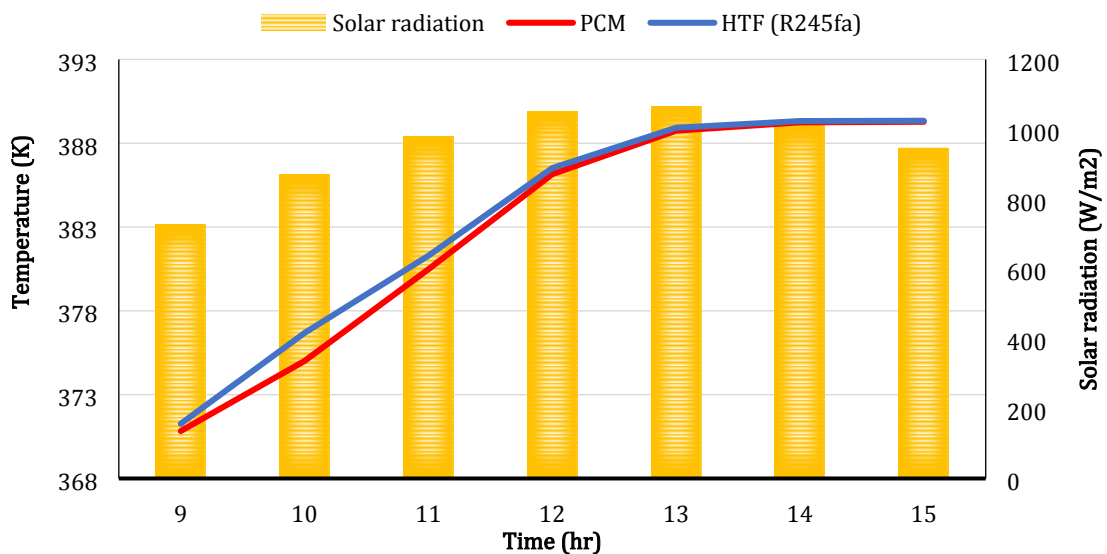
#### 367 4.1.1 Variation in temperature profiles of HTF and PCM during charging mode

368 During charging mode, hourly average daily temperature profiles of both PCM and HTF for ISOS and  
369 DSOS during the hottest week (2<sup>nd</sup> week of June) of the year are shown in [Figure 6](#) and [Figure 7](#)  
370 respectively. It can be seen that HTF temperature shows an increasing and decreasing trend with respect  
371 to the rise and fall of solar radiation. However, it remains constant initially with an initial decrement in  
372 solar radiation. By comparing [Figure 6](#) and [Figure 7](#), it is observed that the number of charging hours  
373 for ISOS and DSOS is found to be 9 and 7 hours, respectively. The number of charging hours is higher  
374 for ISOS because, within the selected range of parametric conditions, HTF temperature cannot reach

375 up to the imposed limit of 390 K. Increment in temperature of PCM for ISOS and DSOS is observed to  
 376 be 7.7 K and 18.5 K, respectively. However, in the case of HTF, these values are found to be 14.8 K  
 377 and 18 K. Moreover, at maximum HTF temperature, the temperature difference between HTF and PCM  
 378 is found to be 10 K and 0 K for ISOS and DSOS, respectively. Hence, it shows that heat transfer between  
 379 HTF and PCM is higher for DSOS in comparison with ISOS. Conclusively, in case of DSOS, there is  
 380 a steep rise in temperature of HTF until it reaches up to the melting point of the PCM under selected  
 381 operating and boundary conditions. Conversely, in case of ISOS, HTF temperature doesn't reach up to  
 382 that limit. This can happen because water has 2.5 times higher value of specific heat capacity as  
 383 compared to R245fa within the given temperature range.



384  
 385 *Figure 6: Variation in temperature profiles of HTF and PCM with solar radiation for ISOS during*  
 386 *charging mode in the hottest week*



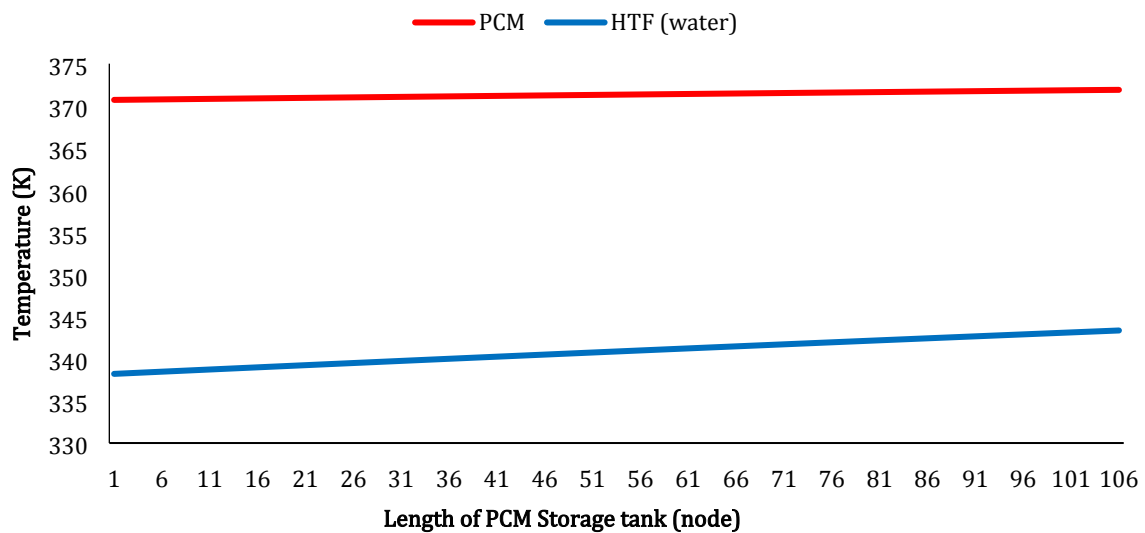
387  
 388 *Figure 7: Variation in temperature profiles of HTF and PCM with solar radiation for DSOS during*  
 389 *charging mode in the hottest week*



390 **4.1.2 Variation in temperature profiles of HTF and PCM during discharging mode**

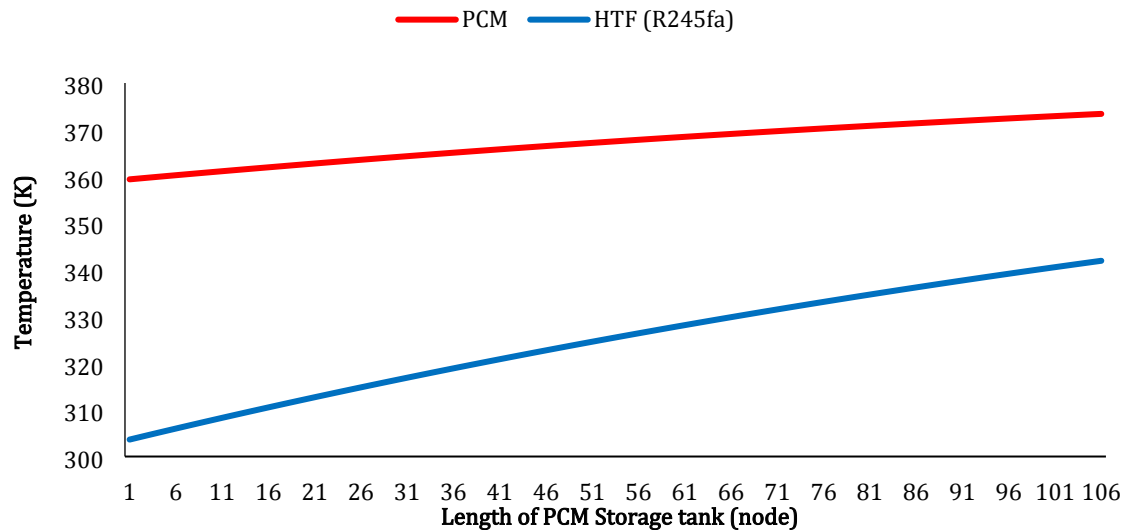
391 A numerical simulation model of the PCM storage tank is developed using MATLAB. The finite  
392 difference method is used to discretize time and space (along one dimension). Therefore, the length of  
393 the PCM storage tank is divided into 105 equally spaced nodes. The simulation time step is selected to  
394 be 1 hour. The model has calculated the temperature of PCM and HTF at each node for every hour  
395 during the whole simulation process. [Figure 8](#) and [Figure 9](#) show variation in hourly average weekly  
396 temperature of PCM and HTF in the hottest week of the year during discharging mode for ISOS and  
397 DSOS respectively. It is observed that the temperature of PCM and HTF generally increases along the  
398 length of the heat storage tank for both ISOS and DSOS. This might happens because the temperature  
399 difference between PCM and HTF is large at the initial node. Therefore, heat transfer from PCM to  
400 HTF is very high at the beginning of discharging process.

401 Therefore, the drop in PCM temperature is larger at that point. Conversely, there is the least temperature  
402 difference between HTF and PCM at the final node. Therefore, heat transfer between HTF and PCM is  
403 comparatively lesser at the final node. Therefore, the drop in PCM temperature is lesser at that point.  
404 Moreover, the temperature difference between a final and initial node of PCM is found to be 14.01 K  
405 and 1.19 K for DSOS and ISOS respectively. Furthermore, an increase in the temperature of HTF along  
406 the PCM storage tank for DSOS is found 7.4 times higher than ISOS. This might happen due to the  
407 higher heat capacity of water as compared to R245fa. However, the relative increment in PCM  
408 temperature with respect HTF decreases along the length of the PCM storage tank.



409

410 *Figure 8: Variation in temperature of PCM & HTF during discharging mode for ISOS in the hottest*  
411 *week*



412

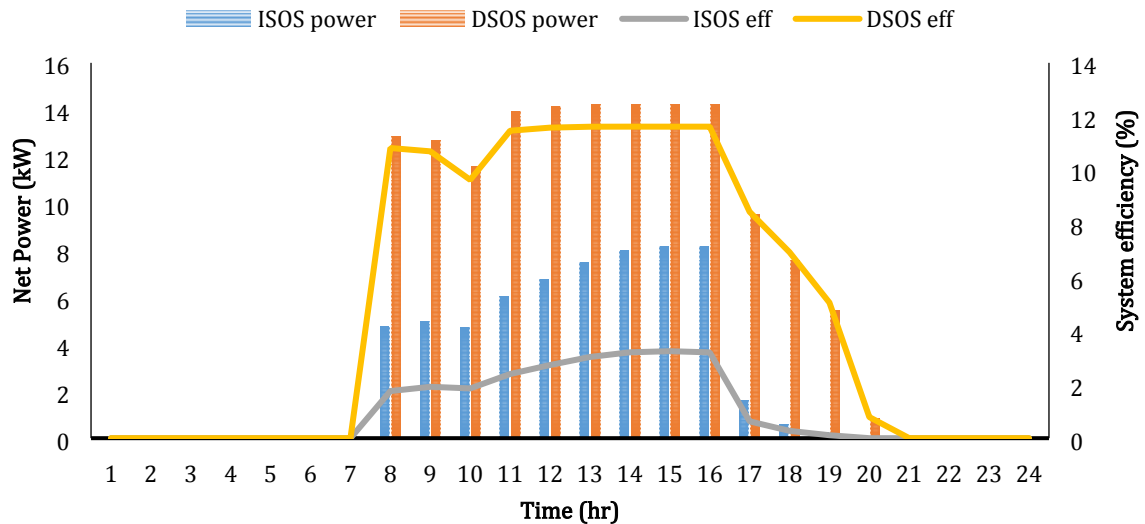
413 *Figure 9: Variation in temperature of PCM & HTF during discharging mode for DSOS in the hottest week*

414 **4.1.3 Variation in system efficiencies and net power output**

415 System efficiency and net power output are the two major parameters that generally describe the  
 416 performance of thermal systems. Therefore, these parameters are calculated for both ISOS and DSOS.  
 417 [Figure 10](#) depicts the results for hourly average daily system efficiency and net power output of ISOS  
 418 and DSOS during the hottest week of the year. In the case of DSOS, the system works from 8:00 till  
 419 21:00 hours, however, for ISOS it works between 7:00 to 20:00. DSOS has resulted in an extra working  
 420 hour than ISOS on an average daily basis. The reduction in working hours for ISOS is due to the weaker  
 421 thermal match between HTF and PCM as shown in [Figure 6](#) and [Figure 8](#). The system efficiency and  
 422 the net power output for DSOS are found to be 5% and 2.4 times higher than ISOS respectively. The  
 423 maximum values of the aforementioned parameters are found at the time instant of 15:00 hours. It  
 424 happens due to the maximum charging of the PCM storage, which occurs at this time instant, as shown  
 425 in [Figure 6](#) and [Figure 7](#). Further, DSOS has achieved 7.5 % higher system efficiency and 6.5 kW extra  
 426 power than ISOS on an average daily basis. Hence, DSOS has demonstrated better thermal performance  
 427 in comparison with ISOS.

428 This might be because of two major reasons: firstly, higher thermal losses occur across evaporator in  
 429 ISOS (research has shown that more than 50 % of exergy losses occur in the evaporator section [18]).  
 430 Secondly, extra power is required to operate the solar pump.

431



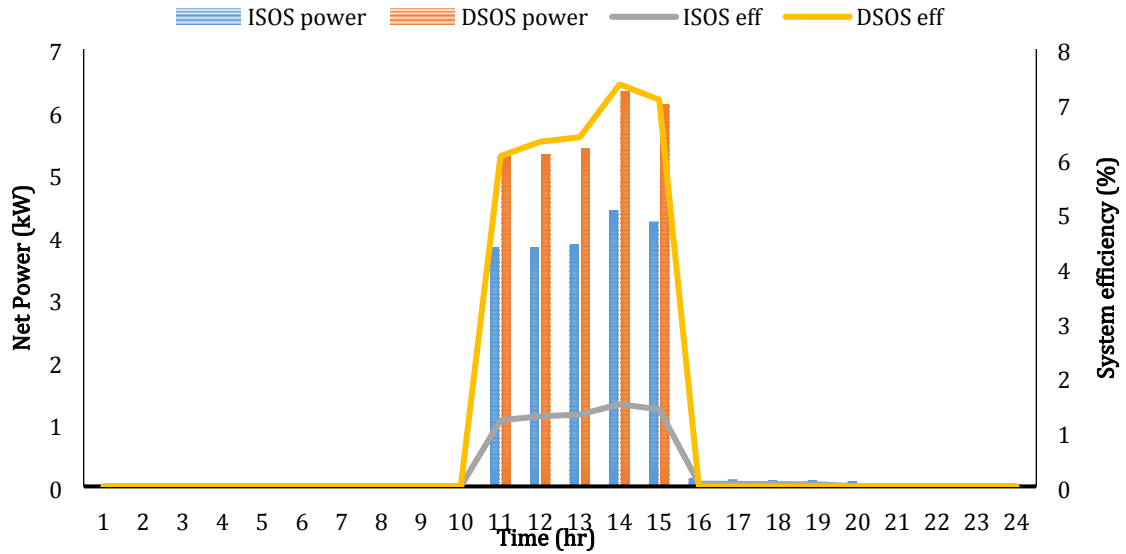
432

433 *Figure 10: Variation in system efficiencies and net power output of DSOS and ISOS during the hottest*  
 434 *week*

435 **4.2 Performance of the coldest week**

436 **4.2.1 Variation in system efficiencies and net power output**

437 [Figure 11](#) shows that the hourly average daily system efficiencies and net power output for ISOS and  
 438 DSOS during the coldest week of the year (1<sup>st</sup> week of January). There are weak solar radiation and  
 439 very low ambient temperature during the coldest week. Both of the systems work between 11:00 to  
 440 15:00. Hence, these weather conditions are not enough to rise the HTF temperature at the outlet of the  
 441 storage tank up to the designed value of 370 K. Therefore, the charging process does not take place in  
 442 both systems. However, both systems have demonstrated an identical trend with the hottest week. DSOS  
 443 has shown higher 4.5 times system efficiency and 1.4 times larger net power output as compared to  
 444 ISOS on an average daily basis. Moreover, DSOS has achieved 1.09 % higher system efficiency and  
 445 0.32 kW extra power than ISOS on an average daily basis. Furthermore, both systems have shown  
 446 maximum system efficiencies and net power at the time instant of 14:00 hour because largest solar  
 447 radiation and highest ambient temperature occur at that time.

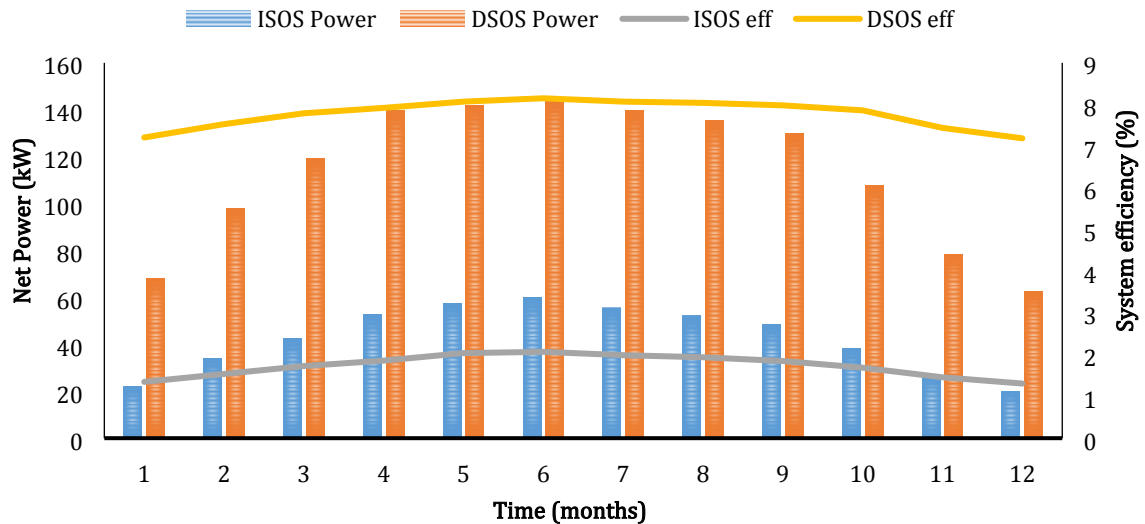


448  
449 *Figure 11: Variation in system efficiencies and net power output of DSOS and ISOS during the*  
450 *coldest week*

451 **4.3 Performance over the month**

452 **4.3.1 Variation in system efficiencies and net power output**

453 [Figure 12](#) shows the daily average monthly system efficiencies and net power output of ISOS and  
454 DSOS, respectively. By comparing [Figure 3](#) and [Figure 12](#), it is observed that both parameters (system  
455 efficiency and net power output) increase and decrease with rising and fall in solar radiation & ambient  
456 temperature. Therefore, both systems have followed similar behavior as seen in the case of weekly  
457 simulation. The maximum value of system efficiencies and net power output are observed in June being  
458 hottest month. Conversely, these values are found to be minimum in January that is the coldest month.  
459 The average system efficiency achieved and daily average net power output delivered by ISOS on  
460 annual basis is observed to be 1.71 % and 34.02 kW, respectively. While DSOS has shown 4.5 times  
461 higher system efficiency and 2.8 times higher net power output on annual basis. Furthermore, DSOS  
462 has shown 6.1% higher system efficiency and 61.5 kW higher average daily net power output than ISOS  
463 on annual basis. Hence, DSOS has shown much better thermal performance than ISOS.

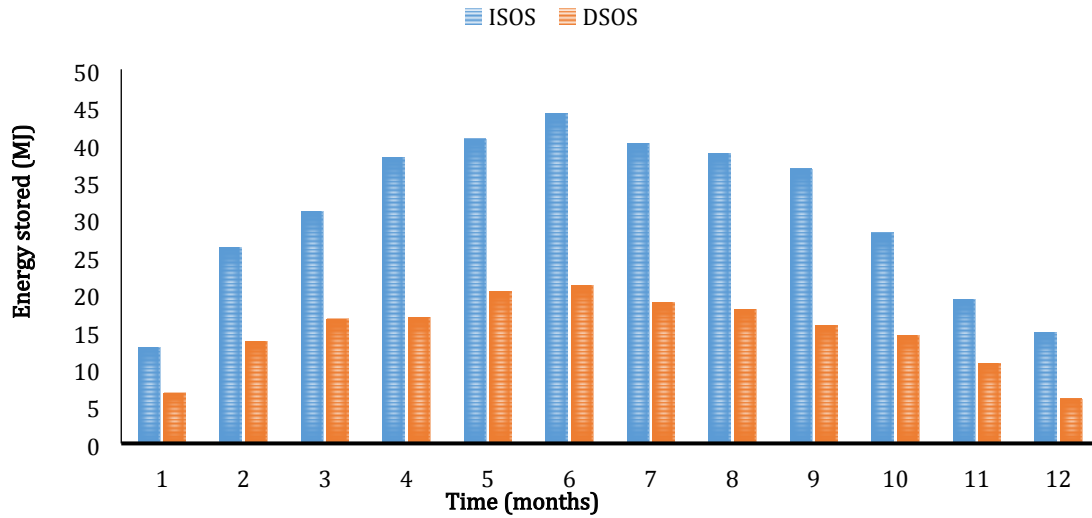


464

465 *Figure 12: Variation in system efficiencies and net power output of DSOS and ISOS on daily average*  
 466 *monthly basis*

467 **4.3.2 Heat stored by PCM during charging mode**

468 The daily average monthly amount of heat stored by the PCM storage tank during charging mode for  
 469 DSOS and ISOS is shown in [Figure 13](#). The PCM storage system is designed to work at PCM melting  
 470 point temperature. However, in the current study, the total amount of heat stored by PCM is the sum of  
 471 both sensible and latent heat. It is observed that the amount of heat stored for both systems increase and  
 472 decrease with respect to rise and fall in solar radiation and ambient temperature as shown in [Figure 3](#)  
 473 and [Figure 13](#). Moreover, maximum and minimum amount of heat stored by PCM is observed during  
 474 June and January, respectively. However, a larger amount of heat is stored by ISOS as compared to  
 475 DSOS. This can happen because the larger amount of heat transfer occurs across ISOS due to a higher  
 476 number of charging hours. The daily average amount of heat stored per annum by PCM storage for  
 477 ISOS is found to be 4.24 MJ more than DSOS. Furthermore, the maximum difference in the average  
 478 daily amount of heat stored for ISOS and DSOS is observed to be 23 MJ that occurs in June. However,  
 479 minimum difference in daily average amount heat stored for both systems is found to be 6 MJ that  
 480 occurs in January.



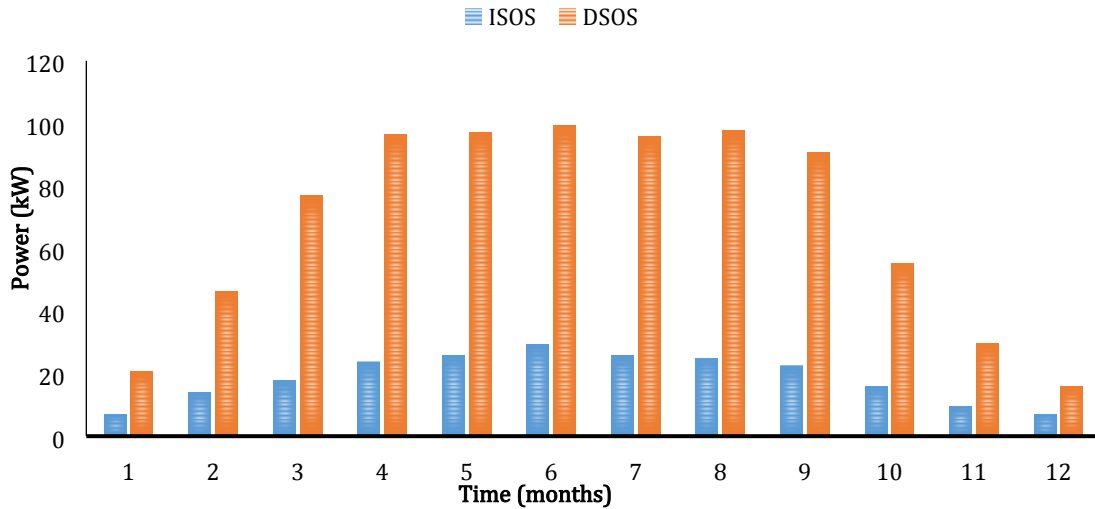
481

482 *Figure 13: Variation in the amount of heat stored by PCM storage tank during charging mode for*  
 483 *DSOS and ISOS on daily average monthly basis*

484 **4.3.3 Power Transferred by PCM to HTF during discharging mode**

485 When solar radiation fall below the imposed limit ( $400 \text{ W/m}^2$ ), both systems undergo discharging mode.  
 486 Power transferred to the HTF from PCM for both systems on a daily average monthly basis during  
 487 discharging mode is shown in [Figure 14](#). It is observed that the amount of power transferred by PCM  
 488 to HTF for both systems increase and decrease with respect to rise and fall in solar radiation and ambient  
 489 temperature as shown in [Figure 3](#) and [Figure 14](#). Furthermore, the maximum and minimum amount of  
 490 power transferred by PCM is observed during June and January, respectively. However, a larger amount  
 491 of power is transferred by PCM for ISOS as compared to DSOS. This might be because of the stronger  
 492 thermal match between PCM and HTF for DSOS as compared to ISOS as shown in [Figure 8](#) and [Figure](#)  
 493 [9](#). Furthermore, the maximum difference in the amount of power transferred by PCM for ISOS and  
 494 DSOS is observed in summer months.

495 However, a minimum difference in power transferred by PCM for both systems is found in the winter  
 496 months. Furthermore, power transferred by PCM to HTF is 4.8 times higher for DSOS as compared to  
 497 ISOS on an annual basis.

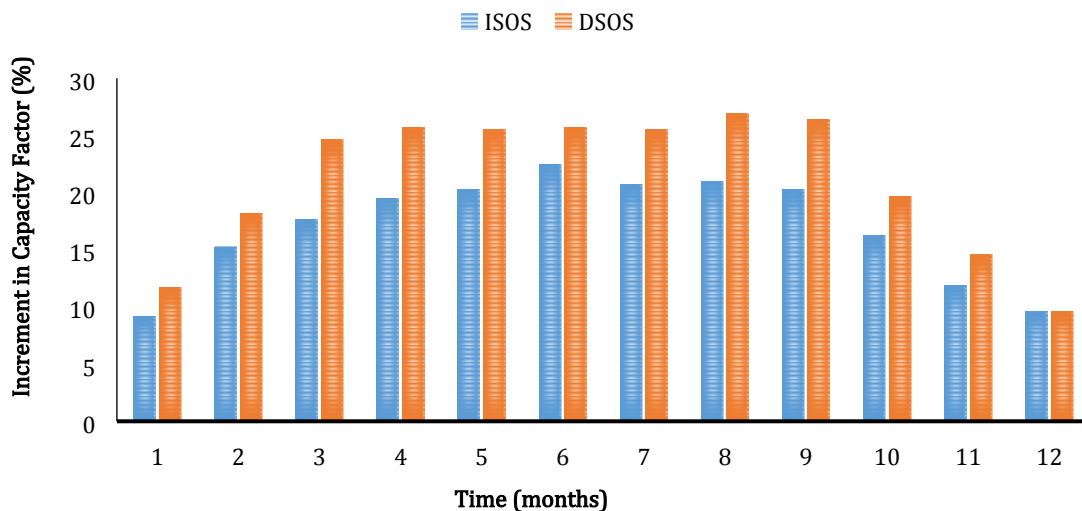


498

499 *Figure 14: Variation in power transferred by PCM to HTF during discharging mode for DSOS and*  
 500 *ISOS on daily average monthly basis*

501 **4.3.4 Increment in capacity factor by employing PCM storage**

502 The capacity factor of both systems increases by employing PCM storage in the systems. [Figure 15](#)  
 503 compares the daily average monthly increment in capacity factor by using PCM storage for both  
 504 systems. The increment in capacity factor usually depends upon the size of the heat storage unit as well  
 505 as operating and boundary conditions. It is observed that it generally increases with increment in solar  
 506 radiation and ambient temperature as shown in [Figure 3](#) and [Figure 15](#). However, in the case of DSOS,  
 507 it has shown higher increment for the summer months having higher solar radiation and ambient  
 508 temperature. Moreover, DSOS has shown higher increment in capacity factor as compared to ISOS.  
 509 Furthermore, with PCM storage, the capacity factor is increased by 17 % and 21.71 % on annual basis  
 510 for ISOS and DSOS respectively.



511

512 *Figure 15: Variation in increment in Capacity Factor by using PCM storage for DSOS and ISOS on*  
513 *daily average monthly basis*

514

## 515 **5 Conclusions**

516 The thermodynamic performance of DSOS and ISOS is compared in this study. A PCM storage tank is  
517 employed in both systems to increase the capacity factor and to assure the stability of power generation.  
518 A numerical mathematical model of PCM storage is developed. The model resulted in temperature  
519 profiles of HTF and PCM that varies with time. Annual dynamic simulations are carried out under time-  
520 varying conditions for both systems. It is concluded from results that DSOS has shown overall better  
521 thermal performance as compared to ISOS. The thermal match between HTF and PCM is stronger in  
522 the case of DSOS in comparison with ISOS. Hence, the temperature difference between HTF and PCM  
523 is found to be 0 K for DSOS and 10 K for ISOS at the maximum HTF temperature. Under given  
524 operating and boundary conditions, DSOS has shown 6.1% higher system efficiency and 61.5 kW  
525 higher daily average net power output than ISOS on an annual basis. Although the annual amount of  
526 heat stored by PCM for ISOS is 1.46 times higher than DSOS in charging mode. This happens might  
527 be due to specific heat capacity of water is almost 3 times higher than R245fa at selected operating and  
528 boundary conditions. However, during discharging mode, annual amount power transferred by PCM to  
529 HTF is 4.8 times higher for DSOS as compared to ISOS because of stronger thermal match of DSOS.  
530 Furthermore, DSOS has achieved 195 working hours higher than ISOS on annual basis. However, the  
531 performance of both systems can be improved significantly by applying more complex logical control.  
532 The future study involves the optimization of latent heat thermal energy storage systems for given  
533 constrains.

## 534 **Acknowledgment**

535 This research work has been supported by the National Natural Science Foundation of China  
536 (51806081), the Natural Science Foundation of Jiangsu Province (BK20180882), the China  
537 Postdoctoral Science Foundation (2018M632241) and the Open Foundation Program of Key  
538 Laboratory of Efficient Utilization of Low and Medium Grade Energy (Tianjin University), the Ministry  
539 of Education of China (201806-402).

540

## 541 **Nomenclature**

542 Symbols

543 A Area [m<sup>2</sup>]  
544 a Heat transfer coefficient  
545 C Specific heat [J/kg/K]  
546 CF Capacity factor



547	D	diameter [m]
548	F	Friction factor
549	H	Volumetric enthalpy [ $\text{J}/\text{m}^3$ ]
550	h	Specific enthalpy [ $\text{kJ}/\text{kg}$ ]
551	I	solar radiation [ $\text{W}/\text{m}^2$ ]
552	m	Mass flow rate [ $\text{kg}/\text{s}$ ]
553	L	Length [m]
554	M	Mass [kg]
555	P	Pressure [bar]
556	Q	Heat transferred [J]
557	q	Energy stored [J]
558	R	Reynolds number
559	T	Temperature [K]
560	W	Work [J]
561	Abbreviations	
562	P	Pump
563	V	Valve
564	CHP	Combined heat and power
565	CPC	Compound parabolic concentrator
566	CSP	Concentrated solar power
567	DSOS	Direct solar organic Rankine cycle system
568	DSG	Direct steam generation
569	DVG	Direct vapor generation
570	EFPC	Evacuated flat plate collector
571	GWP	Global warming potential
572	HTF	Heat transfer fluid
573	ISOS	Indirect solar organic Rankine cycle system
574	LHS	Latent Heat Storages
575	ODP	Ozone depletion potential
576	ORC	Organic Rankine cycle
577	PCM	Phase change material
578	RMB	Ren Min Bi
579	SCHP	Scale distributed solar combined heat and power
580	SEGS	Solar electricity generation system
581	SHS	Sensible heat storage
582	TMY	Typical meteorological year
583	UK	United Kingdom
584	Subscript	
585	amb	Ambient
586	cl	Collector
587	g	Generator
588	i	Inlet
589	mx	Maximum
590	m	melting point
591	HTF	Heat transfer fluid
592	ORC	Organic Rankine cycle
593	o	outlet
594	os	The isentropic process
595	p	Pump
596	PCM	Phase change material
597	sp	Solar pump
598	t	Turbine
599	th	thermal
600	w	with

601	wo	without
602	wf	Working fluid
603	Greek letters	
604	$\beta$	Angle
605	$\lambda$	Latent heat [J/kg/K]
606	$\Delta$	Change
607	$\rho$	Density [kg/m <sup>3</sup> ]
608	$\varepsilon$	Efficiency
609	$\eta$	Thermal efficiency
610		

## 611 References

- 612 [1] W.A. Hermann, Quantifying global exergy resources, *Energy*. 31 (2006) 1685–1702.  
613 doi:10.1016/J.ENERGY.2005.09.006.
- 614 [2] B.F. Tchanche, G. Papadakis, G. Lambrinos, A. Frangoudakis, Fluid selection for a low-  
615 temperature solar organic Rankine cycle, *Appl. Therm. Eng.* 29 (2009) 2468–2476.  
616 doi:10.1016/J.APPLTHERMALENG.2008.12.025.
- 617 [3] J. Wang, Z. Yan, P. Zhao, Y. Dai, Off-design performance analysis of a solar-powered  
618 organic Rankine cycle, *Energy Convers. Manag.* 80 (2014) 150–157.  
619 doi:10.1016/J.ENCONMAN.2014.01.032.
- 620 [4] S. Quoilin, M. Orosz, H. Hemond, V. Lemort, Performance and design optimization of a  
621 low-cost solar organic Rankine cycle for remote power generation, *Sol. Energy*. 85 (2011)  
622 955–966. doi:10.1016/J.SOLENER.2011.02.010.
- 623 [5] Y.-L. He, D.-H. Mei, W.-Q. Tao, W.-W. Yang, H.-L. Liu, Simulation of the parabolic trough  
624 solar energy generation system with Organic Rankine Cycle, *Appl. Energy*. 97 (2012)  
625 630–641. doi:10.1016/J.APENERGY.2012.02.047.
- 626 [6] J. Li, J.Z. Alvi, G. Pei, J. Ji, P. Li, H. Fu, Effect of working fluids on the performance of a novel  
627 direct vapor generation solar organic Rankine cycle system, *Appl. Therm. Eng.* 98 (2016)  
628 786–797. doi:10.1016/j.applthermaleng.2015.12.146.
- 629 [7] X.D. Wang, L. Zhao, J.L. Wang, Experimental investigation on the low-temperature solar  
630 Rankine cycle system using R245fa, *Energy Convers. Manag.* 52 (2011) 946–952.  
631 doi:10.1016/j.enconman.2010.08.022.
- 632 [8] J.L. Wang, L. Zhao, X.D. Wang, An experimental study on the recuperative low  
633 temperature solar Rankine cycle using R245fa, *Appl. Energy*. 94 (2012) 34–40.  
634 doi:10.1016/j.apenergy.2012.01.019.
- 635 [9] X.B. Bu, H.S. Li, L.B. Wang, Performance analysis and working fluids selection of solar  
636 powered organic Rankine-vapor compression ice maker, *Sol. Energy*. 95 (2013) 271–278.  
637 doi:10.1016/j.solener.2013.06.024.
- 638 [10] X.D. Wang, L. Zhao, J.L. Wang, W.Z. Zhang, X.Z. Zhao, W. Wu, Performance evaluation of a  
639 low-temperature solar Rankine cycle system utilizing R245fa, *Sol. Energy*. 84 (2010)  
640 353–364. doi:10.1016/j.solener.2009.11.004.
- 641 [11] Y. Tian, C.Y. Zhao, A review of solar collectors and thermal energy storage in solar  
642 thermal applications, *Appl. Energy*. 104 (2013) 538–553.  
643 doi:10.1016/J.APENERGY.2012.11.051.
- 644 [12] A. Sharma, V.V. Tyagi, C.R. Chen, D. Buddhi, Review on thermal energy storage with phase  
645 change materials and applications, *Renew. Sustain. Energy Rev.* 13 (2009) 318–345.  
646 doi:10.1016/J.RSER.2007.10.005.
- 647 [13] J.Z. Alvi, M. Imran, G. Pei, J. Li, G. Gao, J. Alvi, Thermodynamic comparison and dynamic  
648 simulation of direct and indirect solar organic Rankine cycle systems with PCM storage,  
649 *Energy Procedia*. 129 (2017) 716–723. doi:10.1016/j.egypro.2017.09.103.
- 650 [14] F. Agyenim, N. Hewitt, P. Eames, M. Smyth, A review of materials, heat transfer and phase  
651 change problem formulation for latent heat thermal energy storage systems (LHTESS),  
652 *Renew. Sustain. Energy Rev.* 14 (2010) 615–628. doi:10.1016/J.RSER.2009.10.015.
- 653 [15] S.M. Hasnain, Review on sustainable thermal energy storage technologies, Part I: heat  
654 storage materials and techniques, *Energy Convers. Manag.* 39 (1998) 1127–1138.  
655 doi:10.1016/S0196-8904(98)00025-9.
- 656 [16] D. Zhou, C.Y. Zhao, Y. Tian, Review on thermal energy storage with phase change  
657 materials (PCMs) in building applications, *Appl. Energy*. 92 (2012) 593–605.  
658 doi:10.1016/J.APENERGY.2011.08.025.
- 659 [17] S. Li, H. Ma, W. Li, Dynamic performance analysis of solar organic Rankine cycle with

- 660 thermal energy storage, *Appl. Therm. Eng.* 129 (2018) 155–164.  
661 doi:10.1016/J.APPLTHERMALENG.2017.10.021.
- 662 [18] J. Freeman, K. Hellgardt, C.N. Markides, An assessment of solar-powered organic Rankine  
663 cycle systems for combined heating and power in UK domestic applications, *Appl.*  
664 *Energy*. 138 (2015) 605–620. doi:10.1016/j.apenergy.2014.10.035.
- 665 [19] M. Wang, J. Wang, Y. Zhao, P. Zhao, Y. Dai, Thermodynamic analysis and optimization of a  
666 solar-driven regenerative organic Rankine cycle (ORC) based on flat-plate solar  
667 collectors, *Appl. Therm. Eng.* 50 (2013) 816–825.  
668 doi:10.1016/j.applthermaleng.2012.08.013.
- 669 [20] A.M. Pantaleo, S.M. Camporeale, A. Miliozzi, V. Russo, N. Shah, C.N. Markides, Novel hybrid  
670 CSP-biomass CHP for flexible generation : Thermo-economic analysis and profitability  
671 assessment, *Appl. Energy*. 204 (2017) 994–1006. doi:10.1016/j.apenergy.2017.05.019.
- 672 [21] A.M. Pantaleo, S.M. Camporeale, A. Sorrentino, A. Miliozzi, N. Shah, C.N. Markides, V.A. A,  
673 Hybrid solar-biomass combined Brayton / organic Rankine-cycle plants integrated with  
674 thermal storage : Techno-economic feasibility in selected Mediterranean areas, *Renew.*  
675 *Energy*. (2018) 1–19. doi:10.1016/j.renene.2018.08.022.
- 676 [22] G. Pei, J. Li, J. Ji, Analysis of low temperature solar thermal electric generation using  
677 regenerative Organic Rankine Cycle, *Appl. Therm. Eng.* 30 (2010) 998–1004.  
678 doi:10.1016/j.applthermaleng.2010.01.011.
- 679 [23] P. Gang, L. Jing, J. Jie, Design and analysis of a novel low-temperature solar thermal  
680 electric system with two-stage collectors and heat storage units, *Renew. Energy*. (2011).  
681 doi:10.1016/j.renene.2011.02.008.
- 682 [24] J. Freeman, I. Guarracino, S.A. Kalogirou, C.N. Markides, A small-scale solar organic  
683 Rankine cycle combined heat and power system with integrated thermal energy storage,  
684 *Appl. Therm. Eng.* 127 (2017) 1543–1554. doi:10.1016/j.applthermaleng.2017.07.163.
- 685 [25] M. Iasiello, K. Braimakis, A. Andreozzi, S. Karellas, Thermal analysis of a Phase Change  
686 Material for a Solar Organic Rankine Cycle, *J. Phys. Conf. Ser.* 923 (2017) 012042.  
687 doi:10.1088/1742-6596/923/1/012042.
- 688 [26] G. Manfrida, R. Secchi, K. Stańczyk, Modelling and simulation of phase change material  
689 latent heat storages applied to a solar-powered Organic Rankine Cycle, *Appl. Energy*. 179  
690 (2016) 378–388. doi:10.1016/j.apenergy.2016.06.135.
- 691 [27] S. Lakhani, A. Raul, S.K. Saha, Dynamic modelling of ORC-based solar thermal power plant  
692 integrated with multitube shell and tube latent heat thermal storage system, *Appl.*  
693 *Therm. Eng.* 123 (2017) 458–470. doi:10.1016/j.applthermaleng.2017.05.115.
- 694 [28] Meteonorm, Global Solar Radiation Database - METEONORM, (2015).
- 695 [29] H. Hajabdollahi, A. Ganjehkaviri, M.N. Mohd Jaafar, Thermo-economic optimization of  
696 RSORC (regenerative solar organic Rankine cycle) considering hourly analysis, *Energy*.  
697 87 (2015) 361–368. doi:10.1016/j.energy.2015.04.113.
- 698 [30] F. Calise, M.D. D’Accadia, M. Vicidomini, M. Scarpellino, Design and simulation of a  
699 prototype of a small-scale solar CHP system based on evacuated flat-plate solar collectors  
700 and Organic Rankine Cycle, *Energy Convers. Manag.* 90 (2015) 347–363.  
701 doi:10.1016/j.enconman.2014.11.014.
- 702 [31] E. Günther, S. Hiebler, H. Mehling, R. Redlich, Enthalpy of Phase Change Materials as a  
703 Function of Temperature : Required Accuracy and Suitable Measurement Methods, *Int J*  
704 *Thermophys.* 30 (2009) 1257–1269. doi:10.1007/s10765-009-0641-z.
- 705 [32] F. Mechanics, G. Petrone, L. Cammarata, G. Cammarata, Numerical simulation of pcm  
706 melting process, in: 2012: pp. 469–474.
- 707 [33] B. Zivkovic, I. Fujii, An analysis of isothermal phase change of phase change material  
708 within rectangular and cylindrical containers, *Sol. Energy*. 70 (2001) 51–61.
- 709 [34] F. Calise, C. Capuozzo, A. Carotenuto, L. Vanoli, Thermoeconomic analysis and off-design

710 performance of an organic Rankine cycle powered by medium-temperature heat sources,  
711 Sol. Energy. 103 (2013) 595–609. doi:10.1016/j.solener.2013.09.031.

712 [35] Y. Feng, T. Hung, Y. Zhang, B. Li, J. Yang, Y. Shi, Performance comparison of low-grade  
713 ORCs (organic Rankine cycles) using R245fa, pentane and their mixtures based on the  
714 thermoeconomic multi-objective optimization and decision makings, Energy. 93 (2015)  
715 2018–2029. doi:10.1016/j.energy.2015.10.065.

716 [36] M. Imran, M. Usman, B.-S. Park, H.-J. Kim, D.-H. Lee, Multi-objective optimization of  
717 evaporator of organic Rankine cycle (ORC) for low temperature geothermal heat source,  
718 Appl. Therm. Eng. 80 (2015) 1–9. doi:10.1016/j.applthermaleng.2015.01.034.

719 [37] J. Li, P. Li, G. Pei, J.Z. Alvi, J. Ji, Analysis of a novel solar electricity generation system using  
720 cascade Rankine cycle and steam screw expander, Appl. Energy. 165 (2016) 627–638.  
721 doi:10.1016/j.apenergy.2015.12.087.

722 [38] M. Usman, M. Imran, Y. Yang, D.H. Lee, B.-S. Park, Thermo-economic comparison of air-  
723 cooled and cooling tower based Organic Rankine Cycle (ORC) with R245fa and R1233zde  
724 as candidate working fluids for different geographical climate conditions, Energy. 123  
725 (2017) 353–366. doi:https://doi.org/10.1016/j.energy.2017.01.134.

726 [39] J. Li, J.Z. Alvi, G. Pei, Y. Su, P. Li, G. Gao, J. Ji, Modelling of organic Rankine cycle efficiency  
727 with respect to the equivalent hot side temperature, Energy. 115 (2016) 668–683.  
728 doi:10.1016/j.energy.2016.09.049.

729 [40] F.P. Incropera, T.L. Bergman, A.S. Lavine, D.P. DeWitt, Fundamentals of Heat and Mass  
730 Transfer, 2011.

731